4H-Silicon Carbide as an Acoustic Material for MEMS

Yaoyao Long, Zhenming Liu, and Farrokh Ayazi, *Fellow, IEEE*

***Abstract*—This article discusses the potential of 4H-silicon carbide (SiC) as a superior acoustic material for microelectromechanical systems (MEMS), particularly for high-performance resonator and extreme environments applications. Through a comparison of the crystalline structure along with the mechanical, acoustic, electrical, and thermal properties of 4H with respect to other SiC polytypes and silicon, it is shown that 4H-SiC possesses salient properties for MEMS applications, including its transverse isotropy and small phonon scattering dissipation. The utility and implementation of bonded SiC on insulator (4H-SiCOI) substrates as an emerging MEMS technology platform are presented. Additionally, this article reports on the temperature-dependent mechanical properties of 4H-SiC, including the temperature coefficient of frequency (TCF) and quality factor (*Q*-factor) for Lamé mode resonators. Finally, the 4H-SiC MEMS fabrication including its deep reactive ion etching is discussed. This article provides valuable insights into the potential of 4H-SiC as a mechanoacoustic material and provides a foundation for future research in the field.**

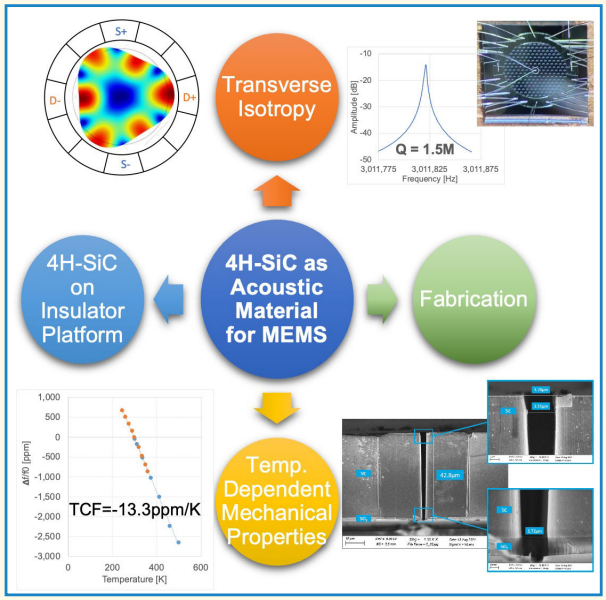

***Index Terms*—4H-SiC, 4H-SiCOI, 4H-SiC high-aspect-ratio (HAR) deep reactive ion etching (DRIE), acoustic materials, elastic anisotropy, elastic constants, frequency split, HAR DRIE, high *Q*-factor, mechanical materials, mechanoacoustic material, microelectromechanical systems (MEMS), MEMS resonators, silicon carbide (SiC), silicon carbide-on-insulator (SiCOI), smart cut, temperature coefficient of frequency (TCF), temperature coefficient of quality factor (TCQ), transverse isotropy.**

I. Introduction

FOR decades, silicon has served as the backbone of the modern electronics industry due to its exceptional electrical, mechanical, and acoustic properties. However, as technological boundaries continue to be pushed, silicon has revealed limitations in high-performance and extreme-environment applications. As an alternative material, monocrystalline silicon carbide (SiC) has emerged as a compound semiconductor of interest with industrial substrates available in various sizes, including 6" and 8" wafers. SiC exhibits a unique combination of mechanical, acoustical, electrical, and chemical properties, including high elastic modulus, high fracture strength, chemical inertness, excellent thermal conductivity, high acoustic velocity, and a wide bandgap, as summarized in Table I [1], [2], [3], [4], [5], [6], [7], [8], [9], [10], [11], [12], [13], [14], [15], [16], [17], [18], [19], [20], [21], [22], [23], [24], [25], [26], [27], [28]. These attributes make SiC a pre-eminent contender in microelectromechanical systems (MEMS) applications, such as radio frequency communications [29], sensors and actuators [3], and nanophotonic structures [30]. Remarkably, the array of characteristics inherent to SiC endows it with high resistance to extreme temperatures, pressure, corrosive chemicals, high power, high radiation, large vibration, and high shock, all of which are typically encountered in harsh environments, such as aerospace, nuclear, oil and gas industries, and defense and automotive applications [13], [31], [32], [33], [34], [35], [36], [37], [38], [39], [40], [41], [42], [43]. Owing to its exceptional characteristics, SiC has garnered burgeoning interest as a mechanoacoustic material for applications that demand top-tier performance even in the most challenging and rigorous conditions.

Manuscript received 20 March 2023; accepted 30 May 2023. Date of publication 5 June 2023; date of current version 13 October 2023. This work was supported in part by Army Research Laboratory under agreement number W911NF-19-2-0345. The U.S. Government is authorized to reproduce and distribute reprints for Government purposes notwithstanding any copyright notation thereon. The views and conclusions contained herein are those of the authors and should not be interpreted as necessarily representing the official policies or endorsements, either expressed or implied, of the Army Research Laboratory (ARL) or the U.S. Government. *(Corresponding author: Yaoyao Long.)*

The authors are with the School of Electrical and Computer Engineering, Georgia Institute of Technology, Atlanta, GA 30308 USA (e-mail: ylong60@gatech.edu; zhenming_liu@gatech.edu; ayazi@gatech.edu).

Digital Object Identifier 10.1109/TUFFC.2023.3282920

Highlights

- **This pioneering study reveals temperature-dependent properties of 4H-SiC, enhancing understanding of its behavior as a superior acoustic material for MEMS.**
- **4H-SiC demonstrates transverse isotropy, superior temperature-dependent mechanical properties, SiCOI, and DRIE availability, highlighting its potential as an advanced acoustic material for MEMS.**
- **This paper emphasizes 4H-SiC's paramount role as an acoustic material for MEMS, revolutionizing high-performance resonators in extreme environments.**

TABLE I
MECHANICAL AND ELECTRICAL PROPERTIES COMPARISON

Property	Unit	(100) Si	(111) Si	(100) 3C-SiC	(0001) 6H-SiC	(0001) 4H-SiC
Density	Kg /m^3	2230	2230	3166	3211	3210
Young's Modulus	GPa	130	174	314	450	481
Fracture Strength	MPa	47.1	31.8	800	--*	200
Yield Strength	GPa	2.7	2.7	12.0	14.3	11.8
Poisson's Ratio	1	0.28	0.26	0.237	0.207	0.205
Volumetric Heat Capacity	10^6 J/ (m^{3}K)	1.58	1.58	2.24	2.22	1.92
Thermal Conductivity	W/cm /°C	1.3	1.48	3.6	3.5	3.7
Thermal Expansion	ppm °C^{-1}	2.6	2.6	2.4	3.4	4.1
Melting Temperature	°C	1412	1412	2830	2830	2830
Acoustic velocity	10^3 m/s	9.1	9.1	11.9	11.9	11.9
Piezoelectric Coefficient e_{33}	10^{-5} C/ cm^2	N/A	N/A	4.0**	4.0	3.4
Bandgap	eV	1.1	1.7	2.4	3.0	3.3
f.Q$_{AKE}$	10^{13} Hz	2 - 3	2 - 3	10 - 50	20 - 60	20 - 60

* No data available in bending test, only compressive facture strength at 24 GPa.
** The e_{33} is under 3C-SiC trigonal structure symmetry with the z-axis along (111).

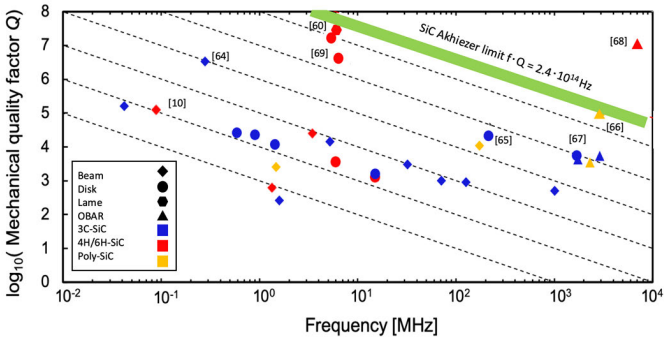

Fig. 1. Benchmark of SiC resonators with ultrahigh Q-factors, where OBAR stands for overtone bulk acoustic resonators [10], [60], [64], [65], [66], [67], [68], [69], updated based on [69].

MEMS technology enables the implementation and integration of microscale mechanical acoustic components and sensors with electronic circuits. Over the years, silicon MEMS sensors and actuators have found numerous applications in various domains, such as healthcare, automotive, defense, and consumer electronics, among others [44], [45], [46], [47], [48], [49], [50], [51], [52]. MEMS resonators use mechanoacoustic vibrations of a lithographically defined micro- or nanostructure with integrated transducers. The quality factor (Q-factor) is an important parameter that characterizes the energy dissipation of a resonator [53]. A high Q-factor indicates that the resonator can store energy efficiently and has a longer ringing time. In other words, the higher the Q-factor, the better the performance of the resonator [54]. In MEMS resonators, a high Q-factor is particularly important because it directly affects the resonator frequency stability, noise level, and sensitivity [55]. A high Q-factor enables the resonator to have a narrow bandwidth, which is beneficial for applications that require precise frequency filtering, such as in wireless communication systems and navigation sensors [53], [56]. Additionally, a high Q-factor reduces the noise level of the resonator, resulting in a higher signal-to-noise ratio (SNR) [57], [58].

Despite the fact that silicon (Si) has been the dominant structural material in high-Q factor applications due to its simplicity of manufacture and possibility to be precisely patterned at the wafer level, monocrystalline SiC as a third-generation semiconductor material boasts exceptional material characteristics that make it a promising material for the development of ultrahigh-Q resonators, exceeding the capabilities of Si. Compared to Si, SiC has higher density, higher Debye velocity, and lower phonon relaxation time. These superior material properties confine the anharmonic phonon–phonon scattering of SiC to be ultralow in the Akhiezer regime with the fQ product of SiC being at least 10-fold greater than that of single crystal silicon (see Table I), which makes SiC a remarkable candidate for ultrahigh-Q applications compared to other mechanoacoustical materials [48], [53], [59]. Fig. 1 provides a graphical summary of measured Q factors from a number of published SiC microresonators spanning a wide frequency range. As shown, the fQ of monocrystalline 4H-SiC resonators has exceeded 1×10^{14} [60], which is already significantly beyond the Akhiezer limit of silicon, which is in the order of 1×10^{13}. Note that the fQ product depends heavily on the value of the Gruüneisen parameter, which is mode dependent and hard to ascertain [60]; therefore, a range is given in Table I.

SiC is a well-known polytypic material with over 250 polytypes [61], and the most prevalent polytypes are 6H, 4H, and 3C [62]. The letters H and C indicate whether the overall lattice type is hexagonal or cubic. The carbon atom

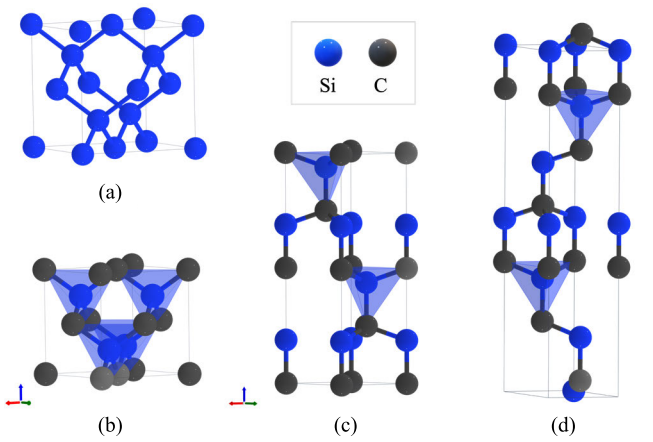

Fig. 2. Unit cell of (a) Si, (b) 3C-SiC, (c) 4H-SiC, and (d) 6H-SiC. The blue atoms represent the Si^{4+} sites, and the black ones are C^{4-} sites. Both Si and 3C-SiC have cubic cells. Si has a diamond structure, and similarly, 3C-SiC has a zincblende structure. Si and 3C-SiC may therefore share similar characteristics. Both 4H-SiC and 6H-SiC have hexagonal cells and similar characteristics; however, 4H-SiC may have slightly less anisotropy due to a more symmetric bond ratio.

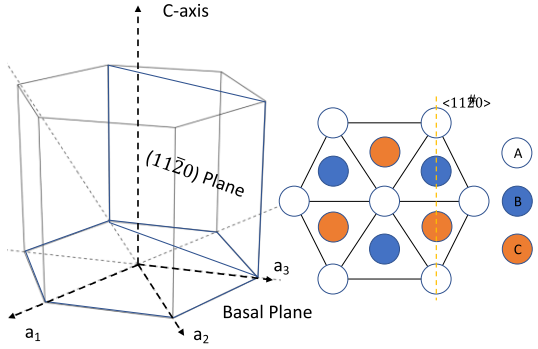

Fig. 3. Hexagonal system of 4H-SiC and the carbon (C) atoms site locations (A, B, and C) in the [1100] plane.

is posited at the center of the tetragonal structure forming by four nearby silicon atoms in all SiC polytypes (polyhedral in Fig. 2). SiC molecules are stacked on top of one another in a particular arrangement to create polytypes. Fig. 3 clearly demonstrates the hexagonal system, where three distinct atom pair double layers stacking positions are labeled as A, B, and C. The stacking sequence of the biatom layers of the SiC structure defines these polytypes [63].

With a stacking sequence of ABC, 3C-SiC [see Fig. 2(b)] is the only cubic crystal lattice form among all the SiC polytypes [63], with only zincblende bonding. The other SiC polytypes consist of a combination of zincblende and wurtzite bonding [70]. 4H-SiC [see Fig. 2(c)] is a moissanite-4H hexagonal structure, with two inequivalent Si^{4+} sites and two inequivalent C^{4-} sites, composed of an equal number of cubic and hexagonal bonds arranged in an ABCB stacking sequence [63]. 6H-SiC [see Fig. 2(d)] is a moissanite-6H hexagonal structure, with three inequivalent Si^{4+} sites and three inequivalent C^{4-} sites, consisting of two-thirds cubic bonds and one-third hexagonal bonds stacked in the order ABCACB [63].

Various structures and stacking sequences will have a substantial effect on the electrical and mechanical properties of SiC polytypes (see Table I), which will have an impact

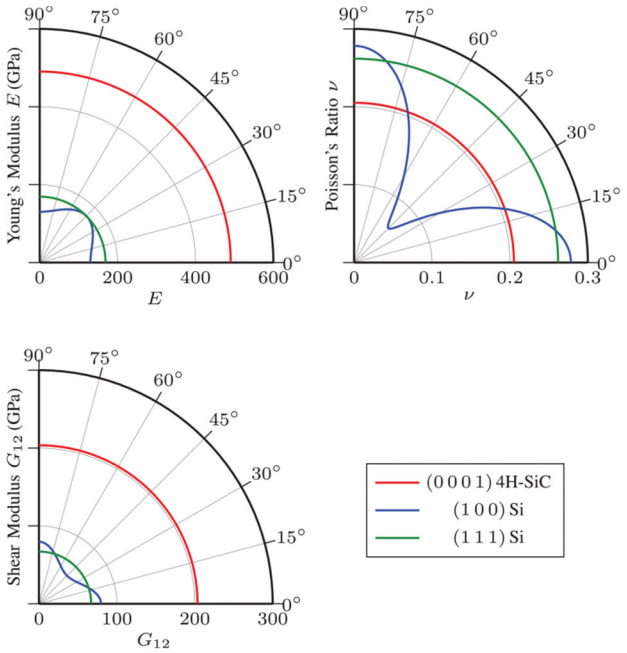

Fig. 4. Elastic anisotropy of monocrystalline Si and 4H-SiC. The in-plane Young's modulus (E), Poisson's ratio (ν), and shear modulus (G_{12}) of (100) Si (similar to 3C-SiC) can vary by up to 45%, while (111) Si and (0001) 4H-SiC are consistent in all directions. The three wafer directions of [100], [112], and [1120] correspond to 0° for Si and 4H-SiC, respectively [72].

on their mechanoacoustic behavior for MEMS. The following section will compare 4H-SiC with the other most common SiC polytypes (3C-SiC and 6H-SiC) as well as Si in terms of the transverse isotropy and the impact on MEMS application. In addition, this work will investigate the elastic anisotropy, elastic constant, and temperature-dependent mechanical properties of 4H-SiC. Finally, the fabrication process for 4H-SiC MEMS devices will be discussed.

II. Transverse Isotropy

Transverse isotropy is a type of crystal anisotropy, in which the material has an axis of symmetry for which the properties of the material are isotropic in the plane orthogonal to this direction. All crystalline materials with a hexagonal crystal system are part of this category [71]. As depicted in Fig. 2, both 4H-SiC and 6H-SiC are hexagonal crystal structures with transverse isotropy. The C-axial is the axis of symmetry, and the material properties are isotropic in the basal plane (0 0 0 1) (see Fig. 3), which is the same as the standard on-axis 4H-SiC wafer. Moreover, 4H-SiC may have a higher degree of symmetric properties compared to 6H-SiC, because cubic and hexagonal bonds are equal in 4H-SiC. In Fig. 4, the in-plane elastic modulus of 4H-SiC is azimuthally invariant in the (0 0 0 1) plane, similar to (1 1 1) Si [72].

However, 3C-SiC is a cubical material without transverse isotropy, elastically similar to (1 0 0) Si. As a result, the 45° in-plane rotation and corresponding basis change must be taken into consideration while developing MEMS devices using substrates like 3C-SiC and (1 0 0) Si [72]. Furthermore, due to the in-plane anisotropy of these materials, the fabrication of consistently high Q width extensional beam resonators will become more challenging, where Q along

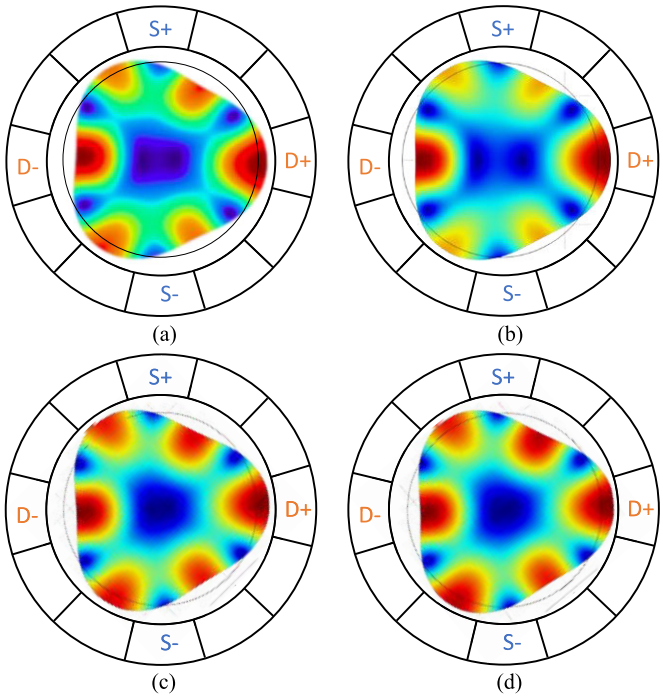

Fig. 5. Anisotropy of (a) (1 0 0) Si and (b) (1 0 0) 3C-SiC leads in nonuniform radial displacement and necessitates the strategic arrangement of electrodes for tuning; (1 0 0) 3C-SiC has less symmetric than (1 0 0) Si, which results in a worse nonuniform. (c) (0 0 0 1) 4H-SiC and (d) (0 0 0 1) 6H-SiC as transverse isotropic materials create symmetric resonant modes and facilitate electrode placements (D+ stands for drive and S+ stands for sense.)

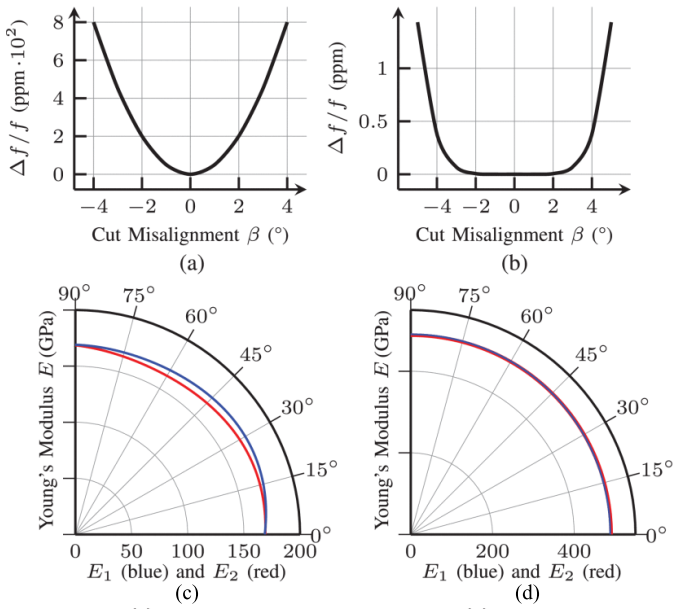

Fig. 6. In degenerate $m = 3$ mode disk resonator, the polar cut misalignment simulation. (a) In (111) Si, significant nondegeneracy occurs with frequency splits reaching nearly 1000 ppm, whereas (b) in 4H-SiC, the frequency split is significantly lower as a function of cut misalignment. The flatness between $-3°$ and $3°$ is likely due to meshing, and it should be noted that the two y-axes are not commensurate with each other. (c) In-plane young's modulus displays a substantial degree of splitting in 4° off-axis (111) Si. (d) Despite being cut at a 4° angle, 4H-SiC remains almost isotropic [72].

[1 1 0] can vary by up to 50% with a 0.1° azimuthal misalignment [72], [73]. However, 4H-SiC can avoid this issue as a transversely isotropic material and keeps the general benefits of SiC. Experimentally, the transverse isotropy of 4H-SiC has been demonstrated in reducing the consequences of misalignment in the piezoresistive effect of p-type epitaxial 4H-SiC [74] and mitigating frequency split in gyroscopic modes of a disk resonator utilizing bulk acoustic wave (BAW) modes [75]. Resonant gyroscopes based on the Coriolis effect depend on both high Q and frequency-degenerate symmetric gyroscopic modes [57]. As such substrates with transverse isotropy such as 4H-SiC are prime candidates for gyroscopic applications.

For cubic material without transverse isotropy like (1 0 0) Si and 3C-SiC, the even-ordered gyroscopic modes will suffer a rather large frequency split as a result of anisotropy, while the odd-ordered modes remain degenerate [72], [76]. Even though the frequency is fully degenerate in odd-order modes of transverse anisotropic materials, the substrate anisotropy still complicates gyroscopic operation and requires rigorous electrode design [57], [77], aiming to minimize and avoid the coupling of the quadrature and frequency mismatch tuning that affects gyroscope stability [49]. As depicted in Fig. 5, the (0 0 0 1) 4H-SiC is a prime candidate for electrode design simplification with its azimuthal isotropy and consistent radial periodicity. In addition and quite importantly, (0 0 0 1) 4H-SiC is considerably more resistant to out-of-plane wafer cut misalignments than even (1 1 1) Si, significantly exceeding wafer specifications [72] (see Fig. 6). Fig. 7 shows the optical picture of a capacitively transduced 4H-SiC disk resonator gyroscope operating at around 3 MHz. Even with the presence of process variations, the design can achieve a frequency split as low as 0.33 ppm at $m = 3$ elliptical mode [75] (see Fig. 7). The Q of this design was measured to be around 1.5M, limited by the substrate decoupling beam network around the central anchor of the device. A slightly larger solid BAW disk resonator without a decoupling network fabricated on a phononic crystal substrate and operating at a higher order mode (5.3 MHz) exhibited a much higher Q of 18M (see Fig. 8).

III. Elastic Anisotropy and Elastic Constant of 4H-SiC

In the last section, 4H-SiC has been demonstrated to be a perfect acoustic mechanical material. Therefore, it is crucial that the anisotropy and elastic constant of 4H-SiC be well comprehended prior to design. Furthermore, as discussed in [11], [60], [69], and [72], attaining an ultrahigh Q is challenging due to anchor losses, which require a solid understanding of the stiffness of 4H-SiC to meet the rigorous frequency requirements of various decoupling strategies.

For hexagonal crystalline materials like 4H-SiC, the anisotropic fourth-order stiffness matrix $\mathbf{C}$ consists of five independent elements, as shown in the following equation (Voigt notation is adopted throughout) [72]:

$$\begin{bmatrix}\sigma_1\\ \sigma_2\\ \sigma_3\\ \sigma_4\\ \sigma_5\\ \sigma_6\end{bmatrix} = \begin{bmatrix} C_{11} & C_{12} & C_{13} & 0 & 0 & 0\\ & C_{11} & C_{13} & 0 & 0 & 0\\ & & C_{33} & 0 & 0 & 0\\ & & & C_{44} & 0 & 0\\ & & & & C_{44} & 0\\ & & & & & C_{66}\end{bmatrix}\begin{bmatrix}\varepsilon_1\\ \varepsilon_2\\ \varepsilon_3\\ \varepsilon_4\\ \varepsilon_5\\ \varepsilon_6\end{bmatrix} \quad (1)$$

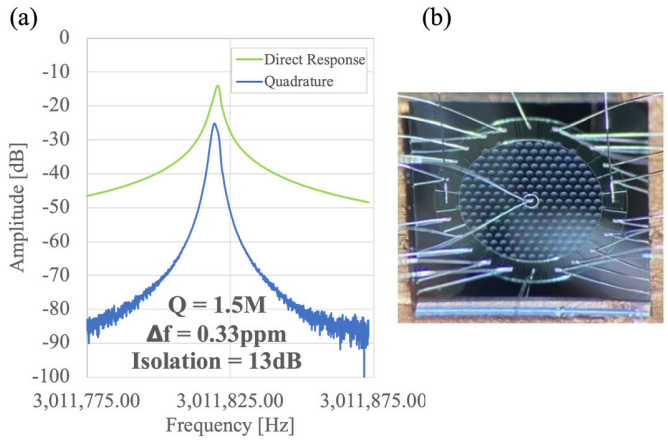

Fig. 7. (a) As-born frequency response of the gyroscopic $m = 3$ BAW mode of a disk resonator, exhibiting a frequency split of 0.33 ppm. (b) Optical image is presented showcasing the wirebonded gyroscope for testing purposes. It is noteworthy that this particular gyroscope represents a significant achievement as the first-ever high-Q disk BAW gyroscope in 4H-SiC, featuring exceptional linearity and a low angle random walk (ARW) of 0.03°/$\sqrt{\text{h}}$ [75].

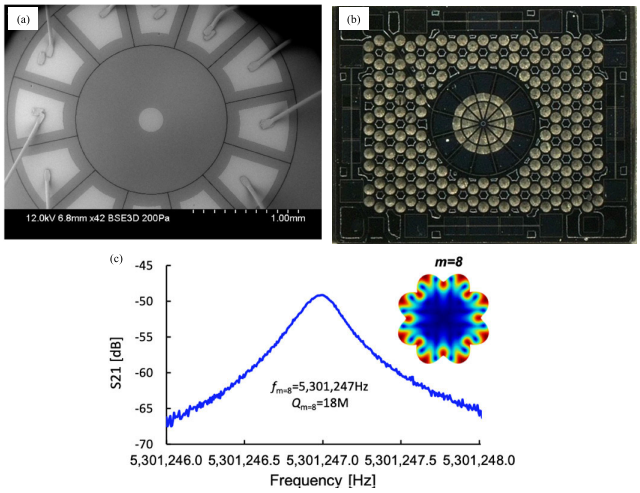

Fig. 8. High-performance 4H-SiC BAW disk gyroscope. (a) SEM of SiC disk resonator. (b) Optical microscope image of the BAW disk gyro. (c) Frequency response of gyroscopic $m = 8$ BAW mode of a 4H-SiC disk resonator [69].

where $C_{66} = (C_{11} - C_{12})/2$. The tensor can also be written with compliance matrix S in terms of Young's modulus (E), shear modulus (G), and Poisson's ratio (v), expressed in the following equation [72]:

$$\begin{bmatrix} \varepsilon_1 \\ \varepsilon_2 \\ \varepsilon_3 \\ \varepsilon_4 \\ \varepsilon_5 \\ \varepsilon_6 \end{bmatrix} = \begin{bmatrix} \frac{1}{E_1} & \frac{-v_{21}}{E_1} & \frac{-v_{31}}{E_3} & 0 & 0 & 0 \\ \frac{-v_{12}}{E_1} & \frac{1}{E_1} & \frac{-v_{31}}{E_3} & 0 & 0 & 0 \\ \frac{-v_{13}}{E_1} & \frac{-v_{13}}{E_1} & \frac{1}{E_3} & 0 & 0 & 0 \\ & & & \frac{1}{G_{23}} & 0 & 0 \\ & & & & \frac{1}{G_{23}} & 0 \\ & & & & & \frac{1}{G_{12}} \end{bmatrix} \begin{bmatrix} \sigma_1 \\ \sigma_2 \\ \sigma_3 \\ \sigma_4 \\ \sigma_5 \\ \sigma_6 \end{bmatrix}. \quad (2)$$

Consequently, the in-plane Young's modulus (E_1) is equal to $1/S_{11}$; shear modulus (G_{12}) is equal to $1/S_{66}$; Poisson's ratio is equal to $v_{12} = -S_{21}/S_{11}$.

As shown in Table II, there is a lack of consensus for the values of elastic constant of bulk monocrystalline 4H-SiC between the measurements by optical Brillouin scattering [78] and Lamé mode square and elliptical mode disk resonator extraction [72] and between the first principal calculations by density functional theory (DFT) [19], [79], [80], [81], [82], [83]. A portion of the nuance in elastic constant may come from the C face having higher values for hardness and elastic modulus than the Si face in 4H-SiC, where Si-core dislocations in the Si face are easier to slide and nucleate than those in the C face [84]. Another may be caused by the variance in substrate composition. Notably, in [59], [60], and [72], the resonators are made by the fusion-bonded monocrystalline 4H SiC-on-insulator (4H-SiCOI) substrate, which consists of a Si substrate and 4H-SiC layer bonded through an intermediate silicon dioxide layer. The 4H-SiCOI substrate has intrinsic advantages over amorphous or epitaxial thin-film substrates, which not only enhance the thickness limitation with amorphous substrates but also mitigate the interfacial defects during the growth process, harming the Q-factor [72]. Additionally, it provides a robust pure monocrystalline 4H-SiC substrate that supports electrically isolated electrodes [69]. Moreover, to accurately analyze and model mechanical behavior of 4H-SiCOI resonators as well as various loss mechanism, including the impact of thermoelastic damping (TED), anchor loss, and Akheiser phonon scattering dissipation (see Fig. 9), it is imperative to comprehend the intricate elastic and material properties of the 4H-SiC as it can be a phenomenal candidate for cutting-edge advancements in MEMS technology, ushering in a new era of precision sensing and measurement with unprecedented levels of accuracy and sensitivity.

Having said that, the Lamé mode square resonator [72] is well-suited for accurately determining the in-plane shear modulus G_{12} and its orientation dependence, as the resonant frequency is purely correlated to the in-plane shear modulus G_{12} in the following equation:

$$f_{\text{Lame}} = \frac{1}{\sqrt{2}\,L}\sqrt{\frac{C_{66}}{\rho}} = \frac{1}{\sqrt{2}\,L}\sqrt{\frac{G_{12}}{\rho}} = \frac{1}{\sqrt{2}\,L}\sqrt{\frac{E_1}{2\rho(1+v_{12})}} \quad (3)$$

TABLE II
BULK MONOCRYSTALLINE 4H-SiC ELASTIC CONSTANTS (GPa)

Ref.	Year		C_{11}	C_{12}	C_{13}	C_{33}	C_{44}	C_{66}
[19]	1995	Cal.	537	156	108	605	170	191
[79]	2007	Cal.	534	96	50	574	171	219
[80]	2014	Cal.	498	91	52	535	159	204
[81]	2015	Cal.	503	92	48	533	161	206
[82]	2021	Cal.	509	94	52	557	164	208
[83]	2022	Cal.	488	105	52	533	158	192
[78]	1997	Exp.	507	108	52	547	159	200
[62] [79]	2020	Exp.	517	110	52	547	159	204

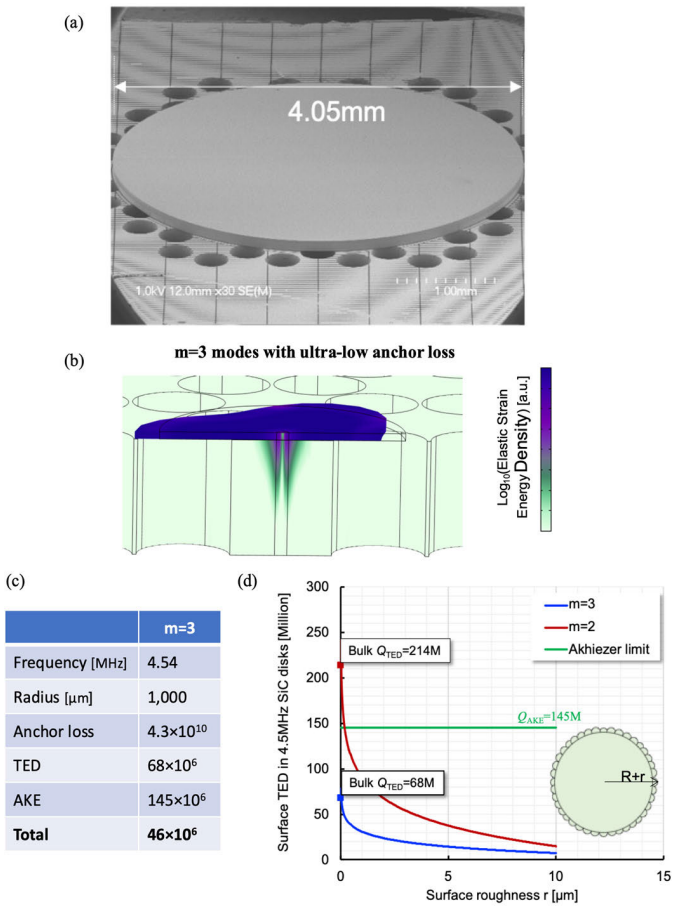

	m=3
Frequency [MHz]	4.54
Radius [μm]	1,000
Anchor loss	4.3×10^{10}
TED	68×10^{6}
AKE	145×10^{6}
Total	**46×10^{6}**

Fig. 9. On the Q analysis of 4H-SiCOI resonators and acoustically engineered substrates. (a) SiC BAW disk resonator. (b) Acoustic isolation is completely achieved in $m = 3$ modes of a solid disk by using phononic crystals in the handle layer with (c) negligible anchor loss ($Q_{\text{Anchor}} \sim 10^{10}$) and a TED-limited Q, with (d) surface-TED identified as the main loss mechanism [85].

where ρ is the density of the structural material and L is the length of the square plate. In addition to that, the ultrahigh Q factor ($Q = 20 \times 10^6$ in Fig. 10) is advantageous in accurately measuring resonant frequencies without any interference from extraneous modes that may affect the desired mode [72]. Meanwhile, the primary displacement of a disk resonator breathing mode is radial, which indicates a significant reliance on C_{11}. The resonant frequency of a solid disk resonator in its mth wineglass mode is expressed in the following equation:

$$f_m = \frac{k_m}{2\pi R}\sqrt{\frac{E}{(1-\upsilon^2)\rho}} \tag{4}$$

where R is the disk outer radius, and E is the effective in-plane axial Young's modulus; the dimensionless frequency parameter k_m is primarily determined by the elasticity of the material; m is the eigenvalue of each mode. Conversely, the elliptical modes of higher order exhibit more shear displacement, indicating a dependence on C_{66}. Besides, the disk resonators are resilient to discrepancies that may arise during fabrication, such as misalignment or variations in pedestal diameter, device thickness, and sidewall tapering [72]. By using information extracted from these two types of resonators, a more precise estimation of the elastic properties of the 4H-SiCOI substrate can be obtained, as listed in the last row of Table II.

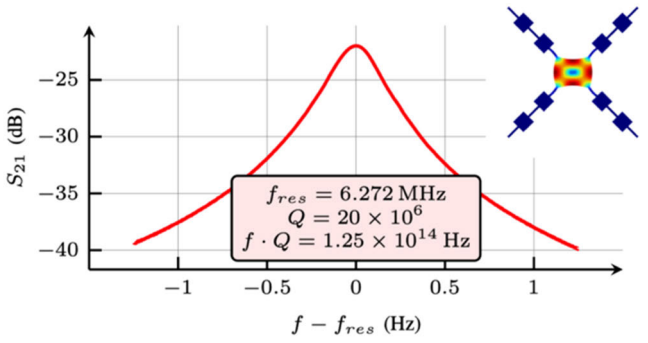

Fig. 10. Utilization of a Lameì mode resonator featuring two unit-PnC cells resulted in a Q value of 20×10^6, which translates to an f Q value of 1.25×10^{14} Hz. This value is more than four times greater than Si's quantum Akhiezer limit [60], [72].

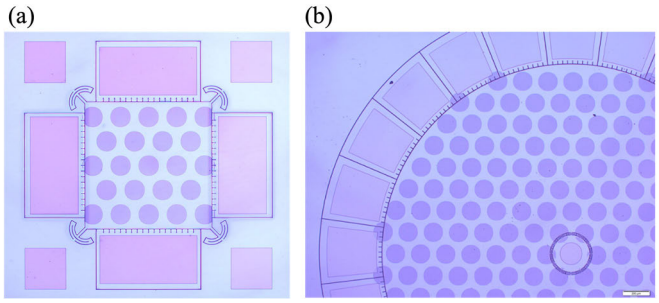

Fig. 11. (a) Lamé mode 4H-SiC resonator and (b) centrally anchored 4H-SiC BAW disk resonators fabricated on SiCOI substrate at Georgia Tech. Both designs have substrate decoupling network to minimize anchor loss. Purple circles are release holes implemented in the handle layer.

IV. Temperature-Dependent Mechanical Properties of 4H-SiC

The temperature coefficient of frequency (TCF) is a significant metric for measuring the frequency stability of resonators, which is the rate of frequency change with temperature compared to a standard frequency. A resonator with a TCF of zero is capable of delivering the utmost stable frequency response amid fluctuations in temperature. Considerable attention has been directed toward examining the frequency response of silicon and quartz crystal resonators under temperature fluctuations, as conventional quartz crystal tuning forks exhibit a TCF value close to zero, with a parabolic coefficient of approximately 0.04 ppm/K^2 [86], making them highly sought-after in applications that demand critical frequency stability. As silicon is the most widely utilized semiconductor, it is desirable to have temperature stable silicon acoustic resonators; however, the typical TCF range for a silicon resonator falls between -20 and -30 ppm/K [87]. Nonetheless, studies exploring the frequency stability of 4H-SiC resonators in the context of temperature fluctuations have been scarce. This section will present a novel investigation into the TCF of 4H-SiC resonators, focusing specifically on Lamé mode and BAW disk resonators.

The 4H-SiC Lamé mode resonator [as depicted in Fig. 11(a)] exhibits a resonant frequency of approximately 6.23 MHz, alongside a Q factor surpassing the 1 million marks at standard room temperature. Notably, the resonator length spans around 935 μm. Based on the resonant frequency of Lamé mode resonator in (3), the TCF of Lamé mode resonator

can be expressed in the following equation:

$$\mathrm{TCF}_{\mathrm{Lame}} = \frac{1}{f_{\mathrm{ref}}}\frac{\partial f_{\mathrm{Lame}}}{\partial T} \approx \frac{1}{2}\frac{\partial f_{\mathrm{Lame}}}{\partial E_1}\frac{\partial E_1}{\partial T} \approx \frac{\mathrm{TCE}}{2} \tag{5}$$

where TCE is the temperature coefficient of Young's modulus of the resonator.

4H-SiC BAW disk resonators with a radius of approximately 1500 μm [see Fig. 11(b)] are also fabricated and tested with respect to $m = 2$, $m = 3$, and breathing modes. The resultant resonant frequencies for each mode, measured at room temperature, are, respectively, determined to be 1.82, 3.01, and 2.56 MHz, with Q-factors exceeding 1 million across all modes.

Similarly, based on the disk resonator frequency in (4), the TCF of BAW disk resonator can be expressed as follows:

$$\mathrm{TCF}_{\mathrm{Disk}} = \frac{1}{f_{\mathrm{ref}}}\frac{\partial f_m}{\partial T} \approx \frac{1}{2}\frac{\partial f_m}{\partial E}\frac{\partial E}{\partial T} \approx \frac{\mathrm{TCE}}{2}. \tag{6}$$

Through the analysis of the TCF using (5) and (6) for the Lamé mode and BAW disk resonator, it can be established that the TCF for both resonators approximates to be half of the thermal coefficient of elasticity (TCE). This phenomenon is attributed to material softening, which leads to a decrease in frequency. Notably, the TCE for 4H-SiC can be calculated using the following equation, as highlighted in [88] and [89]:

$$\mathrm{TCE} = \frac{1}{E_{\mathrm{ref}}}\frac{\partial E}{\partial T} = -\frac{B}{E_{\mathrm{ref}}}\left(1 + \frac{T_0}{T}\right)\exp\left(-\frac{T_0}{T}\right) \tag{7}$$

where E_{ref} is Young's modulus at 0 K, which is 449 GPa for 4H-SiC. B and T_0 are the temperature-independent constants, equal to 0.0324 GPa/K and 640 K for 4H-SiC [88], [89]. At room temperature, the TCE of 4H-SiC is around -26.53 ppm/K, which generated the TCF of both Lamé mode and BAW disk resonator to be around -13.27 ppm/K. In Fig. 12, our TCF measurements for both the Lamé mode and BAW disk resonators are depicted, revealing a TCF of approximately -13.3 ppm/K. Notably, this value closely aligns with the TCE-predicted ones. Specifically, the TCF for the Lamé mode resonators remains consistent at -13.33 ppm/K across the temperature range of -30 ° to 85 °C (243–358 K), as well as the higher temperature range of 27 °C–225 °C (300–498 K). Similarly, the TCF for the $m = 2$, $m = 3$, and breathing modes of the BAW disk resonators was measured at the same temperature ranges, and all modes exhibited a TCF of approximately -13.39 ppm/K. In general, the TCF of 4H-SiC Lamé mode and BAW disk resonators is lower than the 6H-SiC piezoelectric resonators (-18.8 ppm/K) [90] and 6H-SiC torsional resonators (-52 ppm/K) [91]. Additionally, it is worth noting that the TCF of 4H-SiC Lamé mode and BAW disk resonators is slightly less than the value of quartz crystal Lamé mode resonator (19.4 ppm/K) [92] and nearly half of the silicon Lamé mode resonator value (-30 ppm/K) [93].

The temperature coefficient of Q-factor (TCQ) represents the change in the Q-factor with temperature. The significance of TCQ lies in its capacity to influence the stability and precision of resonant circuits across an extensive spectrum of temperatures [56]. In applications such as precision frequency standards, filters, and oscillators, the TCQ must be carefully considered to ensure that the circuit maintains its performance

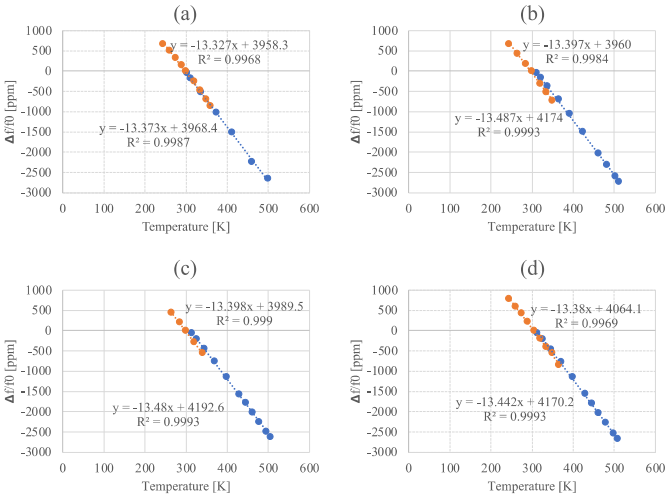

Fig. 12. TCF measurement for various 4H-SiC resonators. (a) Lamé mode square resonator, (b) disk resonator in breathing, (c) $m = 2$, and (d) $m = 3$ BAW mode, indicating a linear TCF of -13.4 ppm/C. The orange data points are measured from -30 °C to 85 °C (243–358 K), and the blue data points are measured from 27 °C to 225 °C (300–498 K).

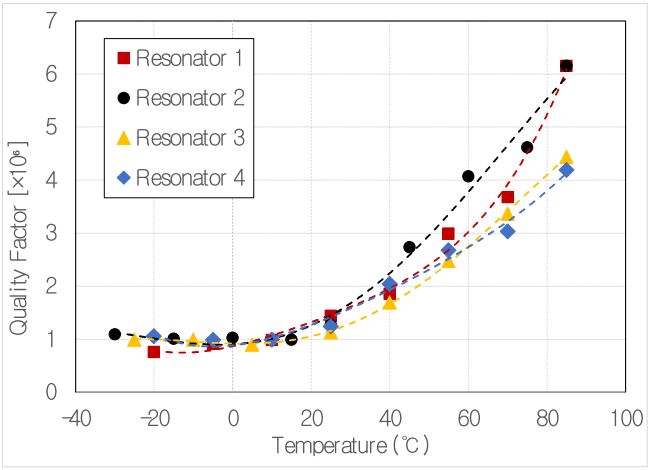

Fig. 13. Measured behavior of Q across temperature for 4H-SiC Lamé mode resonator of Fig. 11(a) in the temperature range of -35 °C to 85 °C (resonators 1–4 have identical design). Further research is needed to explain the positive TCQ in 4H-SiC resonators.

over the required temperature range [56]. The existence of pronounced temperature dependence in the Q-factor of a resonant circuit can offer the possibility of utilizing it as a direct temperature sensing mechanism and employing it as a means of temperature compensation [94]. For the first time, the TCQ of 4H-SiC Lamé mode resonators is reported in this article. As shown in Fig. 13, the Q-factor of the 4H-SiC Lamé mode resonators increases with the increasing temperature from -35 °C to 85 °C, which derives the TCQ a positive value in this range, while Si Lamé mode resonators show an opposite Q-factor behavior with increasing temperature, where the TCQ is negative [95]. It should be noted that centrally anchored 4H-SiC disk resonators also show a positive TCQ trend, while the TCQ of the double-clamped 4H-SiC beam resonator is measured to be negative. Further research is needed to explore the cause of positive TCQ in 4H-SiC resonators, which could be due to surface loss effects.

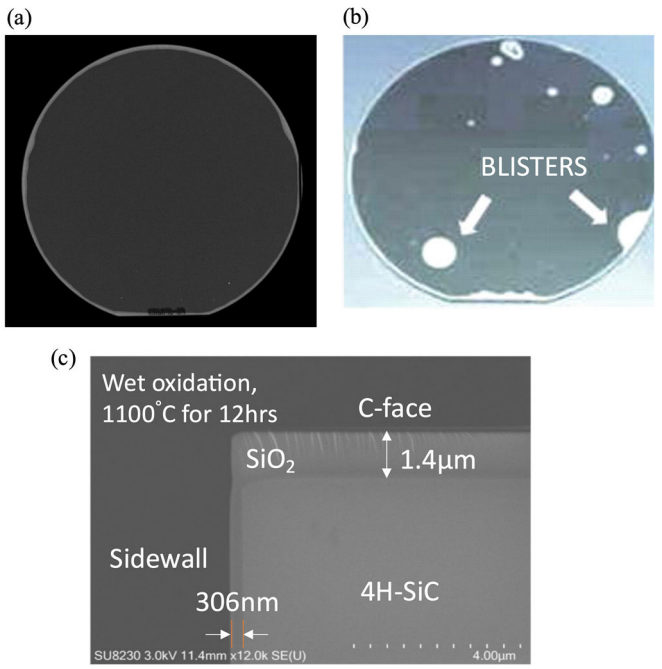

Fig. 14. Si/4H-SiC wafer bonding by (a) oxidation and fusion bonding and (b) Smart-Cut[1] process [99]. (c) Oxidation thickness of the C-face is substantially thicker than the sidewall, indicating C-face has the highest oxidation rate. The C-face is terminated by carbon atoms and Si-face by Si atoms. Nonpolar faces like a-face and m-face have equal number of Si and C atoms.

V. Fabrication

As expounded in Section III, the 4H-SiCOI substrate holds tremendous potential as a versatile technology platform. Integral to the realization of this substrate is the crucial bonding and grinding processes. Notably, there exist two prominent methods for fabricating 4H-SiCOI substrates. The first involves the wet oxidation of 4H-SiC and its fusion bonding with a silicon substrate [see Fig. 14(a)]. Interestingly, it has been discovered that the oxidation rates of the Si-face, C-face, and a-face vary significantly, with the highest on the C-face than a-face and Si-face, and all being consistently slower than in Si [96], as demonstrated in Fig. 14(c). As such, bonding through LPCVD SiO_2 intermediate layers like TEOS has been recently explored with good success. The second method is the Smart-Cut[1] process, entailing hydrogen ion implantation on a SiC wafer, followed by treatment with oxygen plasma, annealing, and splitting. Despite the most application of the Smart-Cut[1] process to 6H-SiC within the SiC materials system [97], recent research has aimed to extend the process to the creation of 4H-SiCOI substrates [98], [99], [100] [see Fig. 14(b)]. However, noteworthy results presented in Fig. 14 indicate that the fusion bonding approach may produce a 4H-SiCOI substrate of superior quality with fewer blisters, while the blister generated during Smart-Cut[1] is due to the presence of a large number of platelets and microsplittings, confined to the depth of maximum hydrogen concentration and the hydrogen diffusion [101]. Besides, due to the limited hydrogen implantation depth, the Smart-Cut[1] process is more suitable for the thin device layer 4H-SiCOI substrates (i.e., less than 1 μm).

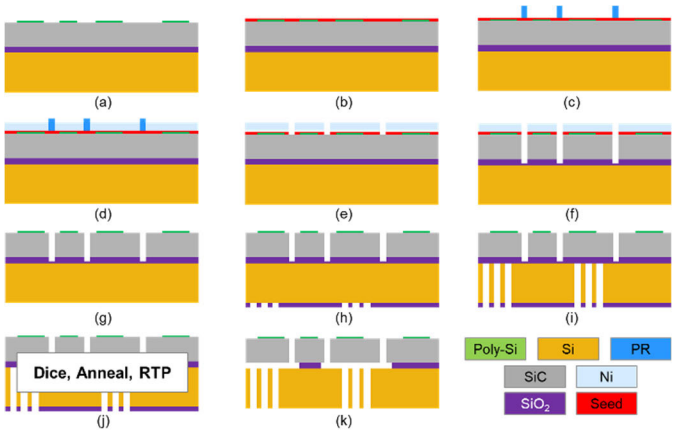

Fig. 15. Cross-sectional schematic view of a generic 4H-SiC micromachining process flow. (a) Polysilicon pad patterning. (b) Cr/Au seed layer deposition. (c) Thick photoresist patterning. (d) Ni maskelectroplating. (e) Ion milling. (f) 4H-SiC DRIE. (g) Ni mask and seed layer removing. (h) Backside PECVDSiO2 patterning. (i) Bosch process. (j) Dicing, annealing. (k) Releasing.

However, in order to realize the full potential of 4H-SiC devices as envisioned, it is critical to achieve precise fabrication as per the design specifications. Nevertheless, in the case of fabricating devices using 4H-SiCOI substrate, there still exist multiple obstacles, including the limitation of thermal budget for processing arising from the coefficient of thermal expansion (CTE) mismatch between Si and SiC and the difficulty of removing NiCxFy passivation by-products in high-aspect-ratio (HAR) deep reactive ion etching (DRIE) of 4H-SiC [59], [102].

The fabrication of 100-mm 4H-SiCOI wafer involved bonding of a 4H-SiC wafer onto a silicon substrate with the aid of TEOS SiO_2 as an intermediate bonding agent, followed by subsequent wafer grinding and polishing. The final 4H-SiCOI wafer is characterized by a device layer of 45 μm thickness comprising 4H-SiC, a buried SiO_2 layer of 3 μm thickness, and a Si handle layer measuring 500 μm in thickness.

Fig. 15(a)–(i) shows the 4H-SiCOI substrate low-temperature wafer-level fabrication process flow, utilizing a three-mask technique. Initially, a thin layer of in situ-doped polysilicon is shaped into electrode pads for wire bonding on the SiC surface [see Fig. 15(a)]. Subsequently, the Cr/Au seed layer is deposited [see Fig. 15(b)], followed by the creation of a SiC trench feature through the thick photoresist pattern [see Fig. 15(c)]. The Ni electroplating process [see Fig. 15(d)] generates a hard mask for HAR DRIE of 4H-SiC, as shown in Fig. 16(a).

Ni is a suitable material for patterning SiC with high fidelity and vertical and smooth sidewalls both in 4H-SiC substrate and 4H-SiCOI [see Fig. 16(b)–(d)], but it presents challenges as the sputtered Ni particles tend to polymerize volatile CxFy etch by-products, resulting in a metallofluorocarbon NiCxFy passivation layer that progressively builds up on the trench sidewalls, highlighted in Fig. 16(b). Unlike the Bosch process used for Si DRIE, the DRIE of 4H-SiC has yet to attain this level of cleanliness. A comprehensive analysis of the DRIE lag, knifing, and notching effects can be found in [59] and [102].

The photoresist is then removed, and the exposed seed layer is eliminated via ion milling [see Fig. 15(e)]. The SiC device

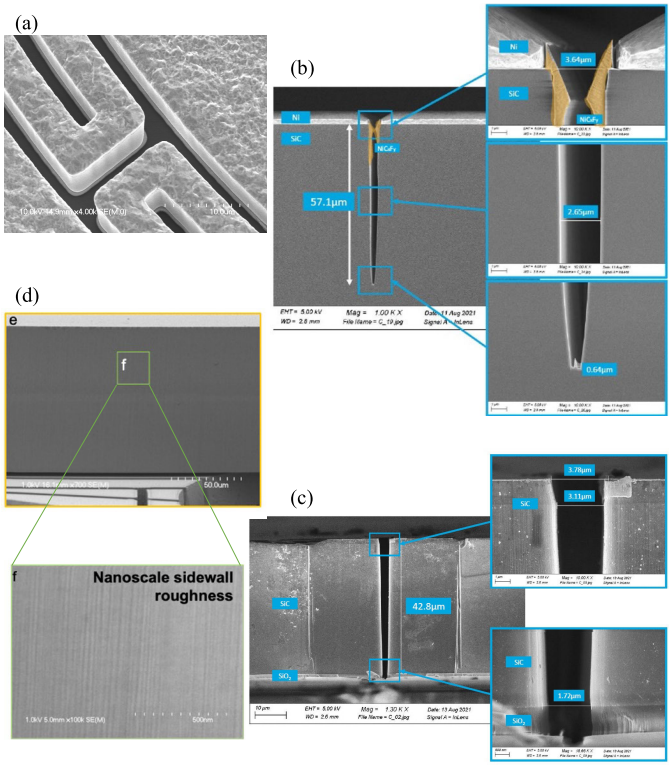

Fig. 16. (a) SEM picture of the 4H-SiC structure with an electroplated nickel mask on the top, after DRIE [102]. (b) Trench created by DRIE on 4H-SiC substrate, where the highlighted parts are nonvolatile NiCxFy passivation, generated during DRIE [102]. (c) Trench created by DRIE on 4H-SiCOI [102]. (d) Vertical and smooth sidewall of the trench after DRIE [69].

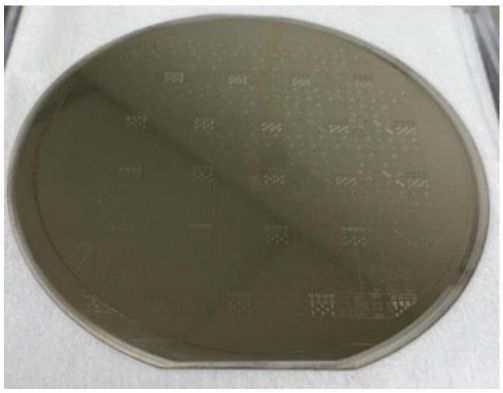

Fig. 17. Picture of a whole 4" 4H-SiCOI wafer having gone through the wafer-level fabrication including SiC DRIE [102].

layer is then etched using a high-density inductively coupled plasma etching instrument designed to etch materials with strong bonds, like Si-C bonds in 4H-SiC, such as the SPTS Synapse^2 module [see Fig. 15(f)]. Fig. 17 depicts the first whole 4H-SiCOI wafer after the DRIE of 4H-SiC. After SiC DRIE, the leftover Ni mask and seed layer are removed [see Fig. 15(g)], and the wafer is inverted for backside processing, beginning with PECVD SiO_2 patterning [see Fig. 15(h)]. The releasing structure for access to the buried oxide is etched in the Si handle layer using the standard Bosch process [see Fig. 15(i)].

Due to the CTE mismatch between Si and SiC in the heterogeneous 4H-SiCOI substrate, the whole 4H-SiCOI wafer cannot be annealed at temperatures substantially above 700 °C without severe wafer warping or cracking. However, in order to prevent delayering of the 4H-SiCOI substrate during HF etching, an annealing duration of 1 h at 1100 °C is necessary for effective densification of the buried oxide layer. Additionally, the high work function of 4H-SiC necessitates the deposition and high-temperature annealing of conductive thin films for the formation of ohmic contact between the aluminum wire bonds and the SiC electrodes and devices [59]. Therefore, the succeeding stages were executed at the die level. Each die underwent annealing at 1100 °C for 7 h, followed by 4 min of rapid thermal processing (RTP) at 1200 °C to establish an ohmic contact between the doped polysilicon and the wideband SiC [see Fig. 15(j)], and released in HF [see Fig. 15(k)].

VI. Conclusion and Future Trends

The monocrystalline 4H-SiC material boasts exceptional mechanical, acoustic, electrical, and thermal properties, thereby positioning it as a highly promising acoustic material for employment in MEMS, an advanced technology platform that operates in demanding environments and high-performance scenarios. This article reveals that the transverse isotropy of 4H-SiC can significantly enhance the design and fabrication of MEMS resonators. Additionally, the elastic anisotropy and elastic constants of both pure 4H-SiC and 4H-SiCOI material systems, which are critical parameters in optimizing device performance, have been summarized herein. The significance of 4H-SiCOI has been underscored. Furthermore, the temperature-dependent mechanical properties, including the 4H-SiC TCF and Q-factor, have been systematically analyzed, as they are fundamental to achieve stable operation in varying thermal conditions. Finally, this article has analyzed and summarized the formation of the 4H-SiCOI substrate and the 4H-SiC MEMS fabrication process, which is a significant step toward showcasing the potential of 4H-SiC as the next-generation acoustic material for MEMS and a platform for extreme environment sensors.

While the 4H-SiC MEMS fabrication process using 4H-SiCOI substrate shows promise, there are still significant challenges to overcome, including lagging, notching, and knifing effects, as well as NiCxFy passivation during HAR DRIE of 4H-SiC. Future research efforts should focus on overcoming these fabrication obstacles, improving masking material, wafer-level packaging, temperature studies, and the integration of sensor arrays for ultrahigh-performance inertial sensors and timing applications. The integration of the high-performance 4H-SiC gyroscope with accelerometers can pave the way for the development of a precision inertial measurement unit (IMU) that can withstand harsh environmental conditions. Given the significant TCF of MEMS resonators that leads to total frequency drifts of approximately 1600 ppm over the industrial temperature range (−40 °C to 85 °C), which is substantially higher than uncompensated quartz crystals [103], the creation of a turnover temperature point, where the local TCF equals zero, can be beneficial to allow for highly stable oscillators to be achieved within the industrial temperature range. By incorporating a heater and temperature sensor, the temperature stability of the 4H-SiC resonator can be maintained at the turnover point, thus enabling the realization of a single-chip oven-controlled crystal oscillator (OCXO) that boasts exceptional

stability and performance in extreme conditions. This, in turn, could facilitate the development of a high-performance single-chip timing and IMU (TIMU) based on 4H-SiC technology. Considering the observation of the TCF turnover temperature point in highly doped Si MEMS resonators at low temperatures [104], there is an eagerness to conduct research on 4H-SiC MEMS resonators to identify opportunities to create zero-TCF and thereby enhance the performance of 4H-SiC as a mechanical acoustic material for a broad range of high-performance applications.

REFERENCES

[1] P. M. Sarro, "Silicon carbide as a new MEMS technology," *Sens. Actuators A, Phys.*, vol. 82, nos. 1–3, pp. 210–218, May 2000, doi: 10.1016/s0924-4247(99)00335-0.

[2] M. Mehregany, C. A. Zorman, S. Roy, A. J. Fleischman, N. Rajan, and C. H. Wu, "Silicon carbide for microelectromechanical systems," *Int. Mater. Rev.*, vol. 45, no. 3, pp. 85–108, Mar. 2000, doi: 10.1179/095066000101528322.

[3] N. G. Wright and A. B. Horsfall, "SiC sensors: A review," *J. Phys. D, Appl. Phys.*, vol. 40, no. 20, pp. 6345–6354, Oct. 2007, doi: 10.1088/0022-3727/40/20/s17.

[4] C.-M. Zetterling, *Process Technology for Silicon Carbide Devices*, 2002.

[5] L. Tong, M. Mehregany, and L. G. Matus, "Silicon carbide as a new micromechanics material," in *Tech. Dig. IEEE Solid-State Sensor Actuator Workshop*, Jun. 1992, pp. 198–201, doi: 10.1109/SOLSEN.1992.228293.

[6] J. B. Casady and R. W. Johnson, "Status of silicon carbide (SiC) as a wide-bandgap semiconductor for high-temperature applications: A review," *Solid-State Electron.*, vol. 39, no. 10, pp. 1409–1422, Oct. 1996, doi: 10.1016/0038-1101(96)00045-7.

[7] X. Qian, P. Jiang, and R. Yang, "Anisotropic thermal conductivity of 4H and 6H silicon carbide measured using time-domain thermoreflectance," *Mater. Today Phys.*, vol. 3, pp. 70–75, Dec. 2017, doi: 10.1016/j.mtphys.2017.12.005.

[8] M. E. Levinshtein, S. Rumyantsev, and M. S. Shur, *Properties of Advanced Semiconductor Materials: GaN, AlN, InN, BN, SiC, SiGe*, 2001.

[9] A. Sadao, *Properties of Group-IV, III–V and II–VI Semiconductors: Adachi/Properties of Group-IV, III–V and II–VI Semiconductors*, 2005, doi: 10.1002/0470090340.

[10] S. Ko, B. Hamelin, J. Yang, and F. Ayazi, "High-Q monocrystalline silicon carbide disk resonators fabricated using DRIE of thick SiC-on-insulator substrates," in *Proc. IEEE Micro Electro Mech. Syst. (MEMS)*, Jan. 2018, pp. 996–999.

[11] J. Yang, B. Hamelin, S. D. Ko, and F. Ayazi, "Ultra-high Q monocrystalline silicon carbidedisk resonators anchored upon a phononic crystal," in *Solid-State, Actuators, Microsyst. Workshop Tech. Dig.*, May 2018, pp. 1–10.

[12] S. Ghaffari et al., "Correction: Corrigendum: Quantum limit of quality factor in silicon micro and nano mechanical resonators," *Sci. Rep.*, vol. 4, no. 1, p. 4331, Mar. 2014, doi: 10.1038/srep04331.

[13] D. G. Senesky, B. Jamshidi, K. Bun Cheng, and A. P. Pisano, "Harsh environment silicon carbide sensors for health and performance monitoring of aerospace systems: A review," *IEEE Sensors J.*, vol. 9, no. 11, pp. 1472–1478, Nov. 2009, doi: 10.1109/JSEN.2009.2026996.

[14] J. Kim, D.-I. Cho, and R. S. Müller, "Why is (111) silicon a better mechanical material for MEMS?" in *Transducers' Eurosensors XV*, E. Obermeier, Ed. Berlin, Germany: Springer, 2001, pp. 662–665.

[15] C. J. Glassbrenner and G. A. Slack, "Thermal conductivity of silicon and germanium from 3 °K to the melting point," *Phys. Rev.*, vol. 134, no. 4A, pp. A1058–A1069, May 1964, doi: 10.1103/physrev.134.a1058.

[16] A. Ziabari, Z. Bian, and A. Shakouri, "Adaptive power blurring techniques to calculate IC temperature profile under large temperature variations," in *Proc. Int. Microelectron. Packag. Soc. (IMAPS) ATW Thermal Manag.*, 2023, pp. 1–15.

[17] M. A. Hopcroft, W. D. Nix, and T. W. Kenny, "What is the young's modulus of silicon?" *J. Microelectromech. Syst.*, vol. 19, no. 2, pp. 229–238, Apr. 2010, doi: 10.1109/jmems.2009.2039697.

[18] Z. Li and R. C. Bradt, "Thermal expansion of the hexagonal (4H) polytype of SiC," *J. Appl. Phys.*, vol. 60, no. 2, pp. 612–614, Jul. 1986, doi: 10.1063/1.337456.

[19] A. P. Mirgorodsky, M. B. Smirnov, E. Abdelmounîm, T. Merle, and P. E. Quintard, "Molecular approach to the modeling of elasticity and piezoelectricity of SiC polytypes," *Phys. Rev. B, Condens. Matter*, vol. 52, no. 6, pp. 3993–4000, Aug. 1995, doi: 10.1103/PhysRevB.52.3993.

[20] R. F. Cook, "Strength and sharp contact fracture of silicon," *J. Mater. Sci.*, vol. 41, no. 3, pp. 841–872, Feb. 2006, doi: 10.1007/s10853-006-6567-y.

[21] M. Zhang, H. M. Hobgood, J. L. Demenet, and P. Pirouz, "Transition from brittle fracture to ductile behavior in 4H–SiC," *J. Mater. Res.*, vol. 18, no. 5, pp. 1087–1095, May 2003, doi: 10.1557/jmr.2003.0150.

[22] G. Kwon et al., "Room-temperature yield and fracture strength of single-crystalline 6H silicon carbide," *J. Mater. Sci.*, vol. 50, no. 24, pp. 8104–8110, Dec. 2015, doi: 10.1007/s10853-015-9379-0.

[23] K. M. Jackson, "Fracture strength, elastic modulus and Poisson's ratio of polycrystalline 3C thin-film silicon carbide found by microsample tensile testing," *Sens. Actuators A, Phys.*, vol. 125, no. 1, pp. 34–40, Oct. 2005, doi: 10.1016/j.sna.2004.10.008.

[24] D. Ravindra, S. Virkar, and J. Patten, "Ductile mode micro laser assisted machining of silicon carbide (SiC)," *Prop. Appl. Silicon Carbide*, vol. 23, pp. 505–535, Jan. 2011.

[25] K. E. Petersen, "Silicon as a mechanical material," *Proc. IEEE*, vol. 70, no. 5, pp. 420–457, May 1982, doi: 10.1109/PROC.1982.12331.

[26] C. Shin, H.-H. Jin, W.-J. Kim, and J.-Y. Park, "Mechanical properties and deformation of cubic silicon carbide micropillars in compression at room temperature," *J. Amer. Ceram. Soc.*, vol. 95, no. 9, pp. 2944–2950, Sep. 2012, doi: 10.1111/j.1551-2916.2012.05346.x.

[27] The Engineering Toolbox. (Apr. 20, 2012). *Elastic Properties and Young Modulus for Some Materials*. [Online]. Available: http://www.engineeringtoolbox.com/young-modulus-d-417.html

[28] S. Kiani et al., "Dislocation glide-controlled room-temperature plasticity in 6H-SiC single crystals," *Acta Mater.*, vol. 80, pp. 400–406, Nov. 2014, doi: 10.1016/j.actamat.2014.07.066.

[29] J. M. Melzak, "Silicon carbide for RF MEMS," in *IEEE MTT-S Int. Microw. Symp. Dig.*, Jun. 2003, pp. 1629–1632.

[30] D. M. Lukin, M. A. Guidry, and J. Vučković, "Integrated quantum photonics with silicon carbide: Challenges and prospects," *PRX Quantum*, vol. 1, no. 2, Dec. 2020, Art. no. 020102.

[31] J. Xia, X. Luo, J. Li, L. Zhu, and Z. L. Wang, "Wear-resisting and stable 4H-SiC/Cu-based tribovoltaic nanogenerators for self-powered sensing in a harsh environment," *ACS Appl. Mater. Interface*, vol. 14, no. 49, pp. 55192–55200, Dec. 2022, doi: 10.1021/acsami.2c15781.

[32] R. G. Azevedo et al., "A SiC MEMS resonant strain sensor for harsh environment applications," *IEEE Sensors J.*, vol. 7, no. 4, pp. 568–576, Apr. 2007, doi: 10.1109/JSEN.2007.891997.

[33] R. G. Azevedo et al., "Silicon carbide coated MEMS strain sensor for harsh environment applications," in *Proc. IEEE 20th Int. Conf. Micro Electro Mech. Syst. (MEMS)*, Jan. 2007, pp. 643–646, doi: 10.1109/MEMSYS.2007.4433166.

[34] T. Liang, W. Li, C. Lei, Y. Li, Z. Li, and J. Xiong, "All-SiC fiber-optic sensor based on direct wafer bonding for high temperature pressure sensing," *Photonic Sensors*, vol. 12, no. 2, pp. 130–139, Jun. 2022, doi: 10.1007/s13320-021-0640-7.

[35] D. Szalkai, "Experimental investigations for development of an innovative SiC sensor for spectrometry of neutrons under harsh environmental conditions," Ph.D. dissertation, Dept. Mech. Eng., Karlsruhe Inst. Technol., Karlsruhe, Germany, 2019, doi: 10.5445/ir/1000096850.

[36] S. L. Garverick, C. Soong, and M. Mehregany, "SiC JFET integrated circuits for sensing and control at temperatures up to 600 °C," in *Proc. IEEE Energytech*, May 2012, pp. 1–6, doi: 10.1109/ENERGYTECH.2012.6304660.

[37] R. Wang, W. H. Ko, and D. J. Young, "Silicon-carbide MESFET-based 400 °C MEMS sensing and data telemetry," *IEEE Sensors J.*, vol. 5, no. 6, pp. 1389–1394, Dec. 2005.

[38] G. P. Neudeck, M. G. Beheim, and C. Salupo, "600 C logic gates using silicon carbide JFET's," NASA Glenn Res. Center, Cleveland, OH, USA, Tech. Rep. E-12172, NAS 1.15:209928, NASA/TM-2000-209928, 2000.

[39] J. B. Casady, W. C. Dillard, R. W. Johnson, and U. Rao, "A hybrid 6H-SiC temperature sensor operational from 25 °C to 500 °C," *IEEE Trans. Compon., Packag., Manuf. Technol., A*, vol. 19, no. 3, pp. 416–422, Sep. 1996, doi: 10.1109/95.536843.

[40] J. Babak, *Poly-Crystalline Silicon Carbide Passivated Capacitive MEMS Strain Gauge for Harsh Environments*, 2008.

[41] A. Ned, A. Kurtz, G. Beheim, F. Masheeb, and S. Stefanescu, "Improved SiC leadless pressure sensors for high temperature, low and high pressure applications," in *Proc. Low High Pressure Appl., 21st Transducer Workshop*, 2004, pp. 1–12.

[42] A. C. Patil, X.-A. Fu, C. Anupongongarch, M. Mehregany, and S. Garverick, "Characterization of silicon carbide differential amplifiers at high temperature," in *Proc. IEEE Compound Semiconductor Integr. Circuits Symp.*, Oct. 2007, pp. 1–4, doi: 10.1109/CSICS07.2007.33.

[43] B. Whitaker et al., "A high-density, high-efficiency, isolated on-board vehicle battery charger utilizing silicon carbide power devices," *IEEE Trans. Power Electron.*, vol. 29, no. 5, pp. 2606–2617, May 2014, doi: 10.1109/TPEL.2013.2279950.

[44] P. Gupta, H. Wen, L. Di Francesco, and F. Ayazi, "Detection of pathological mechano-acoustic signatures using precision accelerometer contact microphones in patients with pulmonary disorders," *Sci. Rep.*, vol. 11, no. 1, p. 13427, Jun. 2021, doi: 10.1038/s41598-021-92666-2.

[45] B. Sang et al., "Detection of normal and paradoxical splitting in second heart sound (S2) using a wearable accelerometer contact microphone," *IEEE Sensors*, Nov. 2022, pp. 1–12, doi: 10.1109/SENSORS52175.2022.9967056.

[46] A. Shokouhmand et al., "Detection of left ventricular ejection fraction abnormality using fusion of acoustic and biopotential characteristics of precordium," in *Proc. IEEE Sensors*, Oct. 2022, pp. 1–4, doi: 10.1109/SENSORS52175.2022.9967355.

[47] P. Gupta, A. Daruwalla, H. R. Wen, and F. Ayazi, "A multi-directional single-proof-mass accelerometer contact microphone (accelophone) with 10 Khz open-loop bandwidth," in *Proc. Int. Solid-State Sensors Actuators Microsyst. Conf.*, 2021, pp. 234–237, doi: 10.1109/transducers50396.2021.9495606.

[48] A. Daruwalla, H. Wen, C.-S. Liu, and F. Ayazi, "Low motional impedance distributed Lamé mode resonators for high frequency timing applications," *Microsyst. Nanoeng.*, vol. 6, no. 1, p. 53, Jun. 2020, doi: 10.1038/s41378-020-0157-z.

[49] H. Wen, A. Daruwalla, C. S. Liu, and F. Ayazi, "A hermetically-sealed 2.9 MHz m=3 disk BAW gyroscope with sub-degree-per-hour bias instability," in *Proc. 33rd Int. Conf. Micro Electro Mech. Syst.* (MEMS), Jan. 2020, pp. 741–744, doi: 10.1109/MEMS46641.2020.9056407.

[50] Z. Liu, H. Wen, and F. Ayazi, "A low-voltage wideband AlN-on-Si gyroscope with sub 10-DPH bias instability mode matched using laser trimming," in *Proc. IEEE Int. Symp. Inertial Sensors Syst. (INERTIAL)*, Mar. 2023, pp. 1–4.

[51] F. Ayazi, H. Wen, A. Daruwalla, and P. Gupta, "Environmentally-robust high-performance silicon TIMU chip," in *Proc. IEEE/ION Position, Location Navigat. Symp. (PLANS)*, Apr. 2020, pp. 16–23.

[52] Y. Long, Z. Liu, C. Wehner, and A. Farrokh, "A centrally-anchored high-Q tunable piezoelectric MEMS resonators FOR wide temperature range RTC," in *Proc. IEEE Int. Symp. Inertial Sensors Syst.*, Mar. 2023, pp. 1–4.

[53] F. Ayazi, L. Sorenson, and R. Tabrizian, "Energy dissipation in micromechanical resonators," *Proc. SPIE*, vol. 8031, pp. 1–12, Apr. 2011, doi: 10.1117/12.884731.

[54] V. B. Braginsky, V. P. Mitrofanov, V. I. Panov, and R. Krotkov, "Systems with small dissipation," *Amer. J. Phys.*, vol. 55, no. 12, pp. 1153–1154, Dec. 1987, doi: 10.1119/1.15272.

[55] R. Mirjalili, H. Wen, D. E. Serrano, and F. Ayazi, "Substrate-decoupled silicon disk resonators having degenerate gyroscopic modes with Q in excess of 1-million," in *Proc. 18th Int. Conf. Solid-State Sensors, Actuators Microsyst.*, Jun. 2015, pp. 15–18.

[56] B. Kim et al., "Temperature dependence of quality factor in MEMS resonators," *J. Microelectromech. Syst.*, vol. 17, no. 3, pp. 755–766, Jun. 2008, doi: 10.1109/jmems.2008.924253.

[57] D. E. Serrano et al., "Substrate-decoupled, bulk-acoustic wave gyroscopes: Design and evaluation of next-generation environmentally robust devices," *Microsyst. Nanoeng.*, vol. 2, no. 1, pp. 1–15, Apr. 2016, doi: 10.1038/micronano.2016.15.

[58] H. Wen, A. Daruwalla, and F. Ayazi, "Resonant pitch and roll silicon gyroscopes with sub-micron-gap slanted electrodes: Breaking the barrier toward high-performance monolithic inertial measurement units," *Microsyst. Nanoeng.*, vol. 3, no. 1, p. 16092, Apr. 2017, doi: 10.1038/micronano.2016.92.

[59] B. Hamelin, J. Yang, and F. Ayazi, "Precision deep reactive ion etching of monocrystalline 4H-SiCOI for bulk acoustic wave resonators with ultra-low dissipation," *J. Electrochem. Soc.*, vol. 168, no. 1, Jan. 2021, Art. no. 017512, doi: 10.1149/1945-7111/abdcc6.

[60] J. Yang, B. Hamelin, and F. Ayazi, "Capacitive lame mode resonators in 65 μm-thick monocrystalline silicon carbide with Q-factors exceeding 20 million," in *Proc. 33rd IEEE Int. Conf. Micro Electro Mech. Syst. (MEMS)*, Vancouver, BC, Canada, Jan. 2020, pp. 226–229.

[61] T. K. Gachovska and J. L. Hudgins, "SiC and GaN power semiconductor devices," in *Power Electronics Handbook*, M. H. Rashid Ed. Oxford, U.K.: Butterworth-Heinemann, 2018, pp. 95–155.

[62] F. Dudley, W. Huang, S. Wang, J. A. Powell, P. Neudeck, and C. Fazi, "White-beam synchrotron topographic analysis of multi-polytype SiC device configurations," *J. Phys. D, Appl. Phys.*, vol. 28, no. 4A, pp. A56–A62, Apr. 1995, doi: 10.1088/0022-3727/28/4a/011.

[63] A. Tesfaye, "SiC semiconductor devices technology, modeling, and simulation," Ph.D. dissertation, Dept. Elect. Eng. Inf. Technol., Vienna Univ. Technol., Vienna, Austria, 2004.

[64] A. R. Kermany, G. Brawley, N. Mishra, E. Sheridan, W. P. Bowen, and F. Iacopi, "Microresonators with Q-factors over a million from highly stressed epitaxial silicon carbide on silicon," *Appl. Phys. Lett.*, vol. 104, no. 8, Feb. 2014, Art. no. 081901, doi: 10.1063/1.4866268.

[65] Z. Wang, J. Lee, and P. X.-L. Feng, "Spatial mapping of multimode Brownian motions in high-frequency silicon carbide microdisk resonators," *Nature Commun.*, vol. 5, no. 1, pp. 1–15, Nov. 2014, doi: 10.1038/ncomms6158.

[66] M. Ziaei-Moayyed, S. D. Habermehl, D. W. Branch, P. J. Clews, and R. H. Olsson, "Silicon carbide lateral overtone bulk acoustic resonator with ultrahigh quality factor," in *Proc. IEEE 24th Int. Conf. Micro Electro Mech. Syst.*, Jan. 2011, pp. 788–792.

[67] X. Lu, J. Y. Lee, and Q. Lin, "High-frequency and high-quality silicon carbide optomechanical microresonators," *Sci. Rep.*, vol. 5, no. 1, pp. 1–12, Nov. 2015, doi: 10.1038/srep17005.

[68] V. J. Gokhale et al., "Epitaxial bulk acoustic wave resonators as highly coherent multi-phonon sources for quantum acoustodynamics," *Nature Commun.*, vol. 11, no. 1, p. 2314, May 2020, doi: 10.1038/s41467-020-15472-w.

[69] B. Hamelin, J. Yang, A. Daruwalla, H. Wen, and F. Ayazi, "Monocrystalline silicon carbide disk resonators on phononic crystals with ultra-low dissipation bulk acoustic wave modes," *Sci. Rep.*, vol. 9, no. 1, p. 18698, Dec. 2019, doi: 10.1038/s41598-019-54278-9.

[70] S. Llmpijumnong and W. R. L. Lambrecht, "Total energy differences between silicon carbide polytypes and their implications for crystal growth," *MRS Proc.*, vol. 492, p. 145, Jan. 1997.

[71] T. T. C. Ting, *Anisotropic Elasticity: Theory and Applications*. New York, NY, USA: Academic, Nov. 2020. Accessed: Jun. 19, 2023, doi: 10.1093/oso/9780195074475.001.0001.

[72] J. Yang, B. Hamelin, and F. Ayazi, "Investigating elastic anisotropy of 4H-SiC using ultra-high Q bulk acoustic wave resonators," *J. Microelectromech. Syst.*, vol. 29, no. 6, pp. 1473–1482, Dec. 2020, doi: 10.1109/jmems.2020.3022765.

[73] A. K. Samarao and F. Ayazi, "Quality factor sensitivity to crystallographic axis misalignment in silicon micromechanical resonators," in *Solid-State, Actuators, Microsyst. Workshop Tech. Dig.*, Hilton Head, SC, USA, Jun. 2010, pp. 479–482.

[74] T.-K. Nguyen et al., "Isotropic piezoresistance of p-type 4H-SiC in (0001) plane," *Appl. Phys. Lett.*, vol. 113, no. 1, Jul. 2018, Art. no. 012104, doi: 10.1063/1.5037545.

[75] Z. Liu, A. Lotfi, M. P. Hardin, and F. Ayazi, "A high-Q solid disk BAW gyroscope in monocrystalline 4H silicon-carbide with sub-PPM as-born frequency split," in *Solid-State, Actuators, Microsyst. Workshop Tech. Dig.*, Hilton Head, SC, USA, 2022, pp. 1–22.

[76] E. Benvenisty and D. Elata, "Frequency matching of orthogonal wineglass modes in disk and ring resonators made from (100) silicon," *IEEE Sensors Lett.*, vol. 3, no. 3, Mar. 2019, Art. no. 2501004, doi: 10.1109/LSENS.2019.2901129.

[77] A. Rahafrooz, D. E. Serrano, D. Younkin, S. Nagpal, I. Jafri, and F. Ayazi, "A 0.5 mm^2 7-MHz capacitive bulk acoustic wave gyroscope in (100) silicon with large dynamic range," in *Proc. IEEE 30th Int. Conf. Micro Electro Mech. Syst. (MEMS)*, Las Vegas, NV, USA, Jan. 2017, pp. 25–28.

[78] K. Kamitani, M. Grimsditch, J. C. Nipko, C.-K. Loong, M. Okada, and I. Kimura, "The elastic constants of silicon carbide: A Brillouin-scattering study of 4H and 6H SiC single crystals," *J. Appl. Phys.*, vol. 82, no. 6, pp. 3152–3154, Sep. 1997, doi: 10.1063/1.366100.

[79] M. Iuga, G. Steinle-Neumann, and J. Meinhardt, "Ab-initio simulation of elastic constants for some ceramic materials," *Eur. Phys. J. B*, vol. 58, no. 2, pp. 127–133, Jul. 2007, doi: 10.1140/epjb/e2007-00209-1.

[80] L. Pizzagalli, "Stability and mobility of screw dislocations in 4H, 2H and 3C silicon carbide," *Acta Mater.*, vol. 78, pp. 236–244, Oct. 2014, doi: 10.1016/j.actamat.2014.06.053.
[81] M. Nuruzzaman, M. Islam, A. Alam, M. A. H. Shah, and A. M. M. T. Karim, "Structural, elastic and electronic properties of 2H- and 4H-SiC," *Int. J. Eng. Res. Appl.*, vol. 5, pp. 48–52, Jan. 2015.
[82] L. Pizzagalli, "Accurate values of 3C, 2H, 4H, and 6H SiC elastic constants using DFT calculations and heuristic errors corrections," *Phil. Mag. Lett.*, vol. 101, no. 6, pp. 242–252, Jun. 2021, doi: 10.1080/09500839.2021.1909167.
[83] S. Ramakers et al., "Effects of thermal, elastic, and surface properties on the stability of SiC polytypes," *Phys. Rev. B, Condens. Matter*, vol. 106, no. 7, Aug. 2022, Art. no. 075201, doi: 10.1103/PhysRevB.106.075201.
[84] X. Liu et al., "Anisotropic deformation of 4H-SiC wafers: Insights from nanoindentation tests," *J. Phys. D, Appl. Phys.*, vol. 55, no. 49, Dec. 2022, Art. no. 494001, doi: 10.1088/1361-6463/ac9535.
[85] B. Hamelin, J. Yang, Z. Liu, and F. Ayazi, "Monocrystalline 4H silicon carbide-on-insulator substrates for NAV-grade planar BAW gyroscopes," in *Proc. IEEE Int. Symp. Inertial Sensors Syst. (INERTIAL)*, Mar. 2021, pp. 1–4, doi: 10.1109/INERTIAL51137.2021.9430480.
[86] A. Valeanu, "Temperature compensation of a tuning fork crystal based on MCP7941X," Microchip Technol., Chandler, AZ, USA, Tech. Rep. DS00001413B/AN1413, 2011.
[87] R. Tabrizian, G. Casinovi, and F. Ayazi, "Temperature-stable high-Q ALN-on-silicon resonators with embedded array of oxide pillars," in *Solid-State, Actuators, Microsyst. Workshop Tech. Dig.*, Jun. 2010, pp. 100–101.
[88] K. Sato, K. Adachi, H. Okamoto, H. Yamaguchi, T. Kimoto, and J. Suda, "High-temperature operation of electrostatically-excited single-crystalline 4H-SiC microcantilever resonators," *Mater. Sci. Forum*, vols. 821–823, pp. 914–918, Jun. 2015.
[89] J. B. Wachtman, W. E. Tefft, D. G. Lam, and C. S. Apstein, "Exponential temperature dependence of young's modulus for several oxides," *Phys. Rev.*, vol. 122, no. 6, pp. 1754–1759, Jun. 1961.
[90] R. Perahia et al., "Piezoelectric single crystal 6H silicon carbide microelectromechanical resonators," in *Solid-State, Actuators, Microsyst. Workshop Tech. Dig.*, May 2018, pp. 75–78, doi: 10.31438/trf.hh2018.20.
[91] R. Yang, Z. Wang, J. Lee, K. Ladhane, D. J. Young, and P. X.-L. Feng, "Temperature dependence of torsional and flexural modes in 6H-SiC microdisk resonators," in *Proc. IEEE Int. Freq. Control Symp. (FCS)*, May 2014, pp. 1–3.
[92] R. S. Strout, "The temperature coefficient of quartz crystal oscillators," *Phys. Rev.*, vol. 32, no. 5, pp. 829–831, Nov. 1928, doi: 10.1103/PhysRev.32.829.
[93] S. Shahraini, R. Abdolvand, and H. Fatemi, "Temperature coefficient of frequency in silicon-based cross-sectional quasi Lamé mode resonators," in *Proc. IEEE Int. Freq. Control Symp. (IFCS)*, May 2018, pp. 1–5.
[94] M. A. Hopcroft et al., "Using the temperature dependence of resonator quality factor as a thermometer," *Appl. Phys. Lett.*, vol. 91, no. 1, Jul. 2007, Art. no. 013505, doi: 10.1063/1.2753758.
[95] G. D. Vukasin et al., "Anchor design affects dominant energy loss mechanism in a Lamé mode MEM resonator," *J. Microelectromech. Syst.*, vol. 29, no. 5, pp. 860–866, Oct. 2020, doi: 10.1109/jmems.2020.3012925.
[96] Y. Song, S. Dhar, L. C. Feldman, G. Chung, and J. R. Williams, "Modified deal grove model for the thermal oxidation of silicon carbide," *J. Appl. Phys.*, vol. 95, no. 9, pp. 4953–4957, May 2004, doi: 10.1063/1.1690097.
[97] R. Yang, Z. Wang, J. Lee, K. Ladhane, D. J. Young, and P. X.-L. Feng, "6H-SiC microdisk torsional resonators in a 'smart-cut' technology," *Appl. Phys. Lett.*, vol. 104, no. 9, Mar. 2014, Art. no. 091906, doi: 10.1063/1.4867866.
[98] Y. Zheng, M. H. Pu, A. L. Yi, X. Ou, and H. Y. Ou, "4H-SiC microring resonators for nonlinear integrated photonics," *Opt. Lett.*, vol. 44, no. 23, pp. 5784–5787, Dec. 2019, doi: 10.1364/ol.44.005784.
[99] M. R. Jennings et al., "Si/SiC heterojunctions fabricated by direct wafer bonding," *Electrochem. Solid-State Lett.*, vol. 11, no. 11, p. H306, 2008, doi: 10.1149/1.2976158.
[100] M. Kim et al., "Transferrable single crystalline 4H-SiC nanomembranes," *J. Mater. Chem. C*, vol. 5, no. 2, pp. 264–268, 2017, doi: 10.1039/c6tc04480h.
[101] B. Aspar et al., "The generic nature of the smart-cut® process for thin film transfer," *J. Electron. Mater.*, vol. 30, no. 7, pp. 834–840, Jul. 2001, doi: 10.1007/s11664-001-0067-2.
[102] A. Lotfi et al., "Wafer-level high-aspect-ratio deep reactive ion etching of 4H-silicon carbide on insulator substrates," in *Proc. Solid-State Sensors, Actuators Microsyst. Hilton Head*, Island, SC, USA, 2022, pp. 5–8.
[103] R. Bechmann, A. D. Ballato, and T. J. Lukaszek, "Frequency temperature characteristics of quartz resonators derived from the temperature behavior of the elastic constants," in *Proc. 16th Annu. Symp. Freq. Control*, Apr. 1962, pp. 77–109, doi: 10.1109/FREQ.1962.199500.
[104] M. Shahmohammadi, B. P. Harrington, and R. Abdolvand, "Turnover temperature point in extensional-mode highly doped silicon microresonators," *IEEE Trans. Electron Devices*, vol. 60, no. 3, pp. 1213–1220, Mar. 2013, doi: 10.1109/TED.2013.2243451.

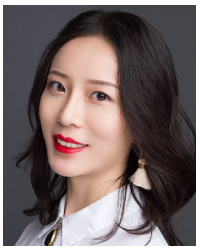

Yaoyao (Emma) Long received the B.S. degree in materials science and engineering from The Ohio State University, Columbus, OH, USA, in 2019, and the M.S. degree in materials science and engineering from Cornell University, Ithaca, NY, USA, in 2021. She is currently pursuing the Ph.D. degree with the School of Electrical and Computer Engineering, Georgia Institute of Technology, Atlanta, GA, USA.

Her research centers around exploring the temperature-dependent properties of micromechanical resonators, encompassing design, fabrication, and the characterization of high-performance MEMS resonators.

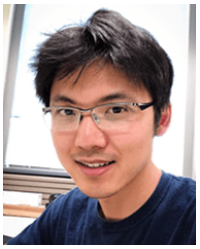

Zhenming Liu received the B.Sc. degree from Rensselaer Polytechnic Institute, Troy, NY, USA, in 2018. He is currently pursuing the Ph.D. degree in electronic and computer engineering with the School of Electrical and Computer Engineering, Georgia Institution of Technology, Atlanta, GA, USA, and joined Integrated MEMS Laboratory (IMEMS) in 2019.

His research focus is on high-performance MEMS resonators in inertial sensing applications.

Farrokh Ayazi (Fellow, IEEE) received the M.S. and Ph.D. degrees in electrical engineering from the University of Michigan, Ann Arbor, MI, USA, in 1997 and 2000, respectively.

He is currently the Regents Entrepreneur and Ken Byers Professor of microsystems at the School of Electrical and Computer Engineering, Georgia Institute of Technology, Atlanta, GA, USA. He is currently the Founder and the Managing Director of StethX Microsystems, Atlanta, a spin-off of his research laboratory that is commercializing smart mechanoacoustic patches for wearable cardiopulmonary applications. He was the Co-Founder and CTO of Qualtré, Marlborough, MA, USA, acquired by Panasonic in 2016, which commercializes bulk acoustic wave (BAW) gyroscopes for personal navigation systems. He holds 67 patents. His main research interest lies in the area of integrated micro- and nano-electromechanical systems (MEMS and NEMS), with a focus on microresonators and inertial sensors.

Dr. Ayazi was the General Co-Chair of the IEEE Micro-Electro-Mechanical-Systems (MEMS) Conference in 2014, held in San Francisco, CA, USA.